

UCLA

UCLA Previously Published Works

Title

Fluids in the Crust. Redox effects on calcite-portlandite-fluid equilibria at for earc conditions: Carbon mobility, methanogenesis, and reduction melting of calcite

Permalink

<https://escholarship.org/uc/item/6hx53271>

Journal

American Mineralogist, 99(8-9)

ISSN

0003-004X

Authors

Lazar, C
Zhang, C
Manning, CE
[et al.](#)

Publication Date

2014-08-01

DOI

10.2138/am.2014.4696

Peer reviewed

FLUIDS IN THE CRUST

Redox effects on calcite-portlandite-fluid equilibria at forearc conditions: Carbon mobility, methanogenesis, and reduction melting of calcite†

CODI LAZAR^{*,1,2}, CHI ZHANG^{1,3}, CRAIG E. MANNING² AND BJORN O. MYSEN¹

¹Geophysical Laboratory, Carnegie Institution of Washington, 5251 Broad Branch Road NW, Washington, D.C. 20015, U.S.A.

²Department of Earth and Space Sciences, University of California, Los Angeles, California 90095, U.S.A.

³Key Laboratory of the Earth's Deep Interior, Institute of Geology and Geophysics, Chinese Academy of Sciences, Beijing, 100029, China

ABSTRACT

Oxygen fugacity (f_{O_2}) is a fundamental parameter that controls carbon mobility in aqueous fluids in geological environments such as subduction zones, where reduced serpentinite fluids have the potential to infiltrate oxidized carbonate-bearing lithologies. Using experiments and calculations, we describe how mineral-fluid equilibria evolve as f_{O_2} decreases in the model Ca-C-O-H system at forearc conditions (300–700 °C and 2–10 kbar). Experimental calcite solubility was constant at f_{O_2} values from quartz-fayalite-magnetite (QFM) to hematite-magnetite (HM). At lower f_{O_2} values of iron-magnetite (IM) or wüstite-magnetite (WM), calcite reacted with H_2 to form methane plus portlandite or melt. These results were consistent with thermodynamic calculations and indicate that carbon mobility, as parameterized by total aqueous carbon ($[C_{TOT}]$), is strongly dependent on f_{O_2} . At constant pressure and temperature, carbon mobility is minimized at oxidizing conditions, where $[C_{TOT}]$ is controlled by calcite solubility. Carbon mobility is maximized at the most reducing conditions because all the carbon in the system is present as CH_4 . An intermediate region of carbon mobility exists in which calcite is stable with a CH_4 -bearing fluid. As pressure increases from 2 to 10 kbar, the f_{O_2} range over which calcite is stable with a methane-rich fluid shifts to more reducing conditions. The variety of geological conditions with the potential for redox enhancement of carbon mobility becomes more restricted with depth. Reduction melting was observed at 700 °C and 6 kbar, and at 650 °C and 10 kbar, due to the partial reaction of calcite to portlandite at conditions above the hydrous melting curve of calcite+portlandite. Although likely metastable in the present experiments, reduction melting may occur in nature whenever H_2 partially reduces carbonate minerals at pressures and temperatures above the hydrous melting curve of calcite+portlandite. Whether it causes melting or not, calcite reduction is likely an important mechanism for abiotic methanogenesis in natural systems such as subduction zone forearcs or similar environments with the potential for interaction of reduced fluids with carbonate minerals. Because calcite solubility at oxidized conditions is already known to increase substantially with pressure, the additional increase in carbon mobility provided by calcite reduction implies that subduction zones may host some of the most carbon-rich aqueous fluids on Earth.

Keywords: Carbon cycle, subduction zones, fluid-rock interaction, serpentinization, forearc mantle, methanogenesis

INTRODUCTION

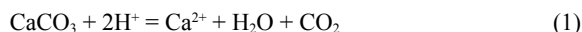
A large portion of inorganic carbon returned to the mantle during subduction is contained in calcite, aragonite, and other carbonate minerals. Much of the carbonate is present as primary clasts and/or matrix cement in pelagic sediments (Sano and Williams 1996), or as hydrothermal veins in metamorphosed oceanic lithosphere (Morgan and Milliken 1996). Along the subduction path, carbon mobility in aqueous fluids is expected to increase dramatically with depth due to the

well-established enhancement of calcite solubility at elevated pressure (P) and temperature (T) (Manning et al. 2013; Facq et al. 2014). For example, experiments in pure water show that the solubility of calcite at 700 °C is ~1000 times higher at 10 kbar than at 1 kbar (Caciagli and Manning 2003). Addition of NaCl amplifies this solubility increase: at 700 °C and 10 kbar, calcite solubility in NaCl- H_2O solutions where $X_{NaCl} = 0.3$ (mole fraction) is about 10 times higher than in pure water at the same P and T (Newton and Manning 2002).

Because carbon speciation depends on redox conditions, calcite solubility is also likely to vary with oxygen fugacity (f_{O_2}). Following Le Chatelier's principle, decreasing f_{O_2} theoretically favors calcite ($CaCO_3$) dissolution, as illustrated by the following reactions:

* E-mail: clazar@ciw.edu

† Special collection papers can be found on GSW at <http://ammin.geoscienceworld.org/site/misc/specialissuelist.xhtml>.



Decreasing f_{O_2} favors CO_2 conversion to CH_4 as reaction 2 moves to the right. This decrease in CO_2 drives reaction 1 to the right, yielding additional consumption of calcite. Following a similar logic in the Ca-S-O-H system, experiments and calculations have shown that anhydrite solubility increases as f_{O_2} decreases from the hematite-magnetite (HM) buffer to the nickel-nickel oxide buffer (NNO) (Newton and Manning 2005). However, no experimental or theoretical study has addressed the effect of f_{O_2} on the solubility of any carbonate mineral, despite the fact that f_{O_2} can vary over many orders of magnitude in common geologic settings.

One such setting is the subduction zone forearc. Geophysical and geological evidence suggests that the forearc mantle is extensively serpentinized (Hyndman and Peacock 2003), and thermodynamic and experimental data indicate that deserpentinization in the slab occurs beneath the forearc (Ulmer and Tromsdorff 1995; Schmidt and Poli 1998). Because olivine-stabilized serpentinization and deserpentinization equilibrate at very low f_{O_2} values (Frost 1985; Peretti et al. 1992), forearcs are likely to contain highly reduced fluids. Such fluids have the potential to infiltrate oxidized carbonate-bearing lithologies such as pelagic sediments (Peacock 1990; Sano and Williams 1996; Lécuyer and Ricard 1999) or completely serpentinized oceanic peridotites (Morgan and Milliken 1996; Schmidt and Poli 1998). In such interactions, low f_{O_2} may amplify the already significant enhancement of calcite solubility by pressure and temperature (Caciagli and Manning 2004). Hydrogen-rich fluids may also destabilize carbonate minerals, as described in recent reports of calcite reduction along serpentinite-marble contacts in the Corsican Alps (Malvoisin et al. 2012; Galvez et al. 2013).

Knowledge of the effect of f_{O_2} on calcite solubility and phase equilibria in the Ca-C-O-H system is critical for understanding carbon mobility in aqueous geological environments such as subduction zones and, more broadly, throughout the global geological carbon cycle. Previous experiments have demonstrated that calcite can be reduced to graphite and hydrocarbons by H_2 gas (Giardini et al. 1968), but it is unclear how such results are applicable to equilibria in supercritical aqueous fluids. Malvoisin et al. (2012) used petrological constraints and thermodynamics to

compute a redox gradient in a natural occurrence of blueschist-grade carbonate reduction in which calcite and quartz reacted with an H_2 -rich fluid to form graphite and wollastonite, but did not attempt a systematic study of f_{O_2} effects over a wider range of conditions. Here, we present a more generalized experimental and theoretical study of the effect of f_{O_2} on calcite solubility and phase equilibria in the model Ca-C-O-H system over a broad range of conditions: 300–700 °C and 2–10 kbar. Our results may aid in the development of integrated models of carbon mobility in subduction zones, oceanic hydrothermal systems, and other aqueous environments of variable redox states.

MATERIALS AND METHODS

Experimental methods

Sand-sized single grain calcite fragments (0.5–1 mg) were cleaved from a rhombohedron of optical-grade spar provided by the Department of Mineral Sciences, Smithsonian Institution (specimen NMNH 144953-34). SEM analyses confirmed high CaCO_3 purity, with a trace Mn concentration of a few hundred parts per million. Grains were gently rounded on sandpaper, cleaned in pure H_2O in a sonicator, and dried at 110 °C. If a rounded grain was intact after an experiment, it was sonicated and reused in a subsequent experiment. Some experiments contained synthetic calcite powder, as confirmed via X-ray diffraction (XRD). In two experiments, calcite powder was composed of isotopically labeled $\text{Ca}^{13}\text{CO}_3$ (>99% isotopic and chemical purity, Sigma-Aldrich). All experiments contained 10–20 mg of ultrapure H_2O (18 M Ω , double-distilled and deionized). Table 1 shows that the molar ratio $\text{H}_2\text{O}:\text{CaCO}_3$ was variable within the suite of experiments, due to the progressive dissolution of reused calcite grains and due to variations in initial water content. As will be explained in the Discussion section, such variations were acceptable because no experiment was performed at an f_{O_2} value at which this range in bulk compositions affected the final equilibrium assemblage.

Most experiments contained an internal oxygen fugacity (f_{O_2}) buffer (Eugster 1957): HM, NNO, quartz-fayalite-magnetite (QFM), Co-CoO (CCO), iron-magnetite (IM), or wüstite-magnetite (WM). All buffer materials were synthetic and pure (>99%). FeO was synthesized in a gas mixing furnace and its identity was confirmed via X-ray diffraction (XRD) analysis; the remaining buffer materials were produced commercially. Each buffer was loaded into a welded Pt capsule (1.5 mm OD) along with ultrapure H_2O . The welded buffer capsule plus calcite and more H_2O were loaded into an outer Au capsule. Two experiments did not contain buffer capsules. In all cases, the outer Au capsule was welded. The success of the weld was confirmed by absence of water loss after a pinch test and heating at 110 °C in a 1-atm oven. For experiments in which calcite solubility was measured, a calcite grain was contained in a second inner Pt capsule to minimize contact with quench material and facilitate post-run removal. This capsule was crimped to permit penetration of the fluid while containing the crystal in case of breakage.

Experiments were performed in piston-cylinder apparatus at UCLA and Geophysical Laboratory at pressures of 6–15 kbar and temperatures of 500–700 °C. At UCLA, the assembly was a graphite heater in an NaCl pressure medium.

TABLE 1. Mineral stability experiments in the Ca-C-O-H system

Run	Buffer	$\Delta\log$ QFM	\log f_{O_2}	T (°C)	P (kbar)	Time (h)	Starting morphology	$\text{H}_2\text{O}:\text{CaCO}_3$ (molar)	Run products ^a	GC-MS
CG10	WM	-5.8	-29.2	500	3	27	Single grain	81	P, C	
CU25	IM	-5.6	-26.1	550	10	20	Single grain	382	P	
CU28	IM	-5.6	-26.1	550	10	21	Single grain	109	P, C	
CU29	IM	-5.6	-26.1	550	10	22	Labeled powder	43	P	$^{13}\text{CH}_4$
CG06	WM	-4.7	-22.0	650	10	1	Single grain	106	P, M	
CG09	WM	-4.7	-22.0	650	10	4	Single grain	65	P	
CU13	WM	-4.4	-20.4	700	10	2	Single grain	603	P, C	
CG02	CCO	-1.2	-18.5	650	10	4	Single grain	42	C	
CG04	CCO	-1.2	-18.5	650	10	24	Single grain	85	C	
CU15	CCO	-0.7	-23.7	500	6	3	Single grain	314	C	
CU35	NNO	-0.1	-20.0	550	15	23	Unlabeled powder	15	C	
CU23	unbuff ^b	0.2	-20.3	550	10	20	Single grain	419	C	
CU42	NNO	0.2	-18.6	600	10	44	Single grain	671	C	
CU45	NNO	0.3	-22.2	500	10	72	Labeled powder	11	C	no $^{13}\text{CH}_4$
CU17	unbuff ^b	0.5	-22.5	500	6	3	Single grain	106	C	

^a Fluid-saturated run products: C = calcite, P = portlandite, M = melt. ^b Unbuffered; f_{O_2} approximately NNO.

At Geophysical Laboratory, the assembly was a graphite heater in an MgO-talc pressure medium with a Pyrex sleeve. During quench, temperatures decreased to below 100 °C within 15–20 s. One experiment (CG10) was performed at 3 kbar in a cold-seal hydrothermal apparatus with an H₂O pressure medium with quench times to below 100 °C in 20–30 min.

After each experiment, the outer Au capsule was cleaned and weighed to confirm that no water was lost during the experiment. Each capsule was then carefully punctured and dried overnight at 110 °C. For solubility experiments, the dry capsule was weighed to determine the mass of H₂O in the experimental fluid. Each buffer capsule was weighed to confirm that no water was lost, punctured to confirm the presence of liquid water, and then opened to confirm the existence of the required solid phases for each buffering assemblage. Experiments containing buffers that did not contain all phases required for equilibrium were rejected. Success of the NNO, QFM, HM, and CCO buffers was confirmed optically. IM and WM were confirmed via XRD. Unbuffered experiments, performed at UCLA, were assumed to equilibrate at an f_{O_2} value near NNO, based on previous experimental measurements in the same assembly type (Newton and Manning 2005).

The product calcic phases (calcite, portlandite, and/or quench melt) were identified using various techniques: binocular microscopy, polarized microscopy, immersion oils, Raman spectroscopy, and scanning electron microscopy (SEM). Note that the model system Ca-C-O-H features portlandite (Ca(OH)₂) as a representative calcite reduction product. In natural systems, e.g., the Malvoisin et al. (2012) serpentinite-marble reaction zone, the presence of additional components such as Si and Al would lead to the formation of more chemically complex calcic products such as wollastonite or grossular.

In the solubility experiments, the crimped Pt capsule containing the run product was retrieved and weighed. Solubility was computed from measurements of calcite weight loss and of the mass of coexisting H₂O (see Caciagli and Manning 2003, Eq. 5). Mass measurements were performed with a UMX2 ultramicrobalance (1 s.d. = ±0.2 µg).

Volatile species for two experiments were extracted by puncturing the capsules in a gas vial under a slight vacuum. The headspace contents were then extracted with a locking gas syringe and injected into a gas chromatograph mass spectrometer (GCMS) equipped with a CarbonPlot column for qualitative analysis (Fig. 1).

Thermodynamic calculations

Thermodynamic calculations in the Ca-C-O-H system were performed using a modified version of EQBRM (Anderson and Crerar 1993). The following phases and fluid species were considered: calcite, portlandite, H₂O(l), O₂(g), H₂(aq), CO₂(aq), CO(aq), CH₄(aq), CaCO₃(aq), Ca²⁺, CaHCO₃⁺, CaOH⁺, H⁺, OH⁻, HCO₃⁻, and CO₃⁻. Standard states were selected to be unit activity of the pure phase at any P and T for minerals and H₂O(l), unit activity of the hypothetical one molal solution referenced to infinite dilution for aqueous species, and unit activity of the pure phase at 1 bar and any T for O₂(g). The standard state Gibbs free energies of calcite and portlandite were taken from the model of Dolejš and Manning (2010) based on previous solubility experiments (Walther 1986; Walther and Long 1986; Fein and Walther 1989; Caciagli and Manning 2003). The P - T range of the previous calcite experiments overlaps the conditions of the current study; however, because the previous portlandite experiments were limited to 300–600 °C and 1–3 kbar, the Dolejš-Manning model was necessary to extrapolate Ca(OH)₂ solubilities to 700 °C and/or 10 kbar. Standard state Gibbs free energies for aqueous and gaseous species were taken from the GEOPIG slop98.dat database (Helgeson et al. 1978; Shock et al. 1989, 1997). Log K values at 10 kbar (Table 2) for aqueous species were extrapolated from the 5 kbar limit of slop98.dat by assuming linearity with the log density of water (see Manning 2013).

Activity of H₂O was assumed to be unity. However, this assumption becomes invalid at low f_{O_2} due to the increased concentrations of reduced fluid species. Therefore, the calculations were limited to f_{O_2} values above which the mole fraction of H₂O was 0.9 or greater. Activity coefficients for charged species were computed using the Davies equation with an extended term of 0.3 (Davies 1962). Activity coefficients of neutral species were assumed to be unity. Manning (2013) showed that speciation calculations at high P and T are insensitive to choice of activity model at the ionic strengths of this study.

The bulk composition of the Ca-C-O-H system was fixed by defining the molar ratio, H₂O:CaCO₃, of the system. This is effectively a closed-system water-rock ratio and facilitates comparison of experiments with thermodynamic calculations.

A series of graphite-fluid equilibria in the system C-O-H were computed, following French (1966). In addition to graphite, the following gaseous species were considered: H₂O, H₂, O₂, CH₄, CO, and CO₂. Standard states were selected to be unit activity of the pure phase at any P and T for graphite and at 1 bar and

any T for gaseous species. Standard state Gibbs free energies were taken from the slop98.dat database. Fugacity coefficients were computed using the CORK equation of state (Holland and Powell 1991). Ideal mixing of nonideal species was assumed (Lewis and Randall 1923).

RESULTS

Run products

The product solid phases were calcite, portlandite, quenched melt, or a combination thereof (Tables 1 and 2). No graphite or other C-bearing phases were observed. Aqueous fluid was always in excess. Calcite was clear and morphologically similar to the initial rounded grain, although rhombohedral dissolution/precipitation features were visible via SEM. Portlandite was conspicuously platy, faintly iridescent, and clear. Quenched melt was white due to the presence of microcrystals formed during quench (Wyllie and Tuttle 1960). Several textural features of the quenched melt were consistent with liquid rheology at P

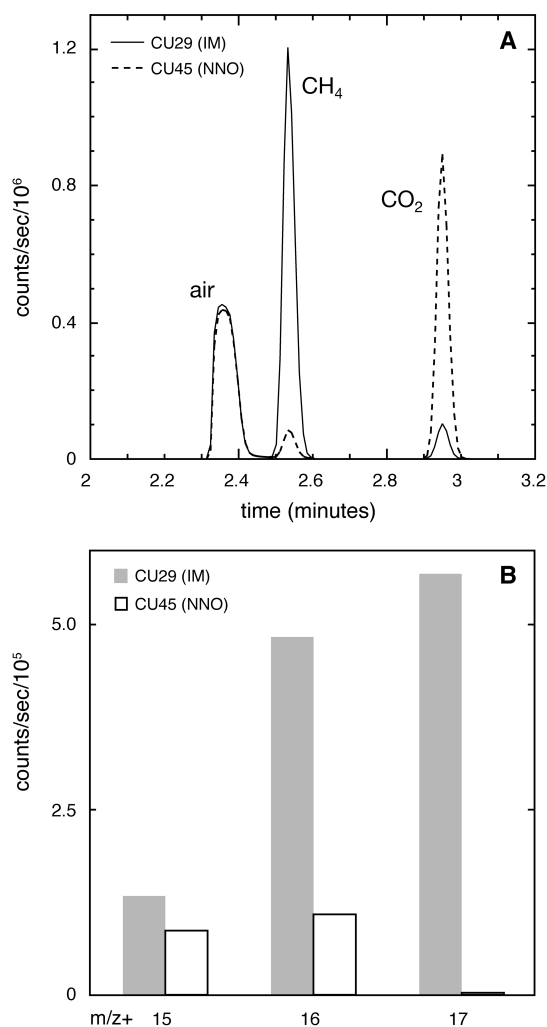


FIGURE 1. Gas chromatograph mass spectrometer analyses of Ca¹³CO₃ experiments CU45 (f_{O_2} = NNO) and CU29 (f_{O_2} = IM): (a) gas chromatograms; (b) mass spectra of CH₄.

TABLE 2. Log K values used in thermodynamic calculations

	300 °C, 2 kbar	300 °C, 10 kbar	500 °C, 2 kbar	500 °C, 10 kbar	650 °C, 10 kbar	700 °C, 10 kbar
$\text{H}_2\text{O} = \text{H}^+ + \text{OH}^-$	-10.26	-8.70	-10.23	-7.95	-7.74	-7.70
$\text{CO}_2 + \text{H}_2\text{O} = \text{H}^+ + \text{HCO}_3^-$	-7.53	-5.90	-9.41	-7.76	-9.15	-9.76
$\text{HCO}_3^- = \text{H}^+ + \text{CO}_3^{2-}$	-10.12	-7.75	-11.69	-8.89	-9.74	-10.05
$\text{CaCO}_3(\text{cc}) = \text{Ca}^{2+} + \text{CO}_3^{2-}$	-11.02	-7.02	-16.25	-9.49	-10.81	-11.43
$\text{CaHCO}_3 = \text{Ca}^{2+} + \text{HCO}_3^-$	-3.00	-3.00	-5.02	-3.95	-4.75	-5.05
$\text{CaCO}_3(\text{aq}) = \text{Ca}^{2+} + \text{CO}_3^{2-}$	-5.65	-4.74	-7.84	-4.91	-5.03	-5.43
$\text{CaOH}^+ = \text{Ca}^{2+} + \text{OH}^-$	-3.55	-1.85	-5.61	-2.67	-1.96	-1.85
$\text{CH}_4 + 3\text{CO}_2 = 4\text{CO} + 2\text{H}_2\text{O}$	-17.90	-20.68	-10.36	-12.61	-8.38	-6.89
$\text{CH}_4 + \text{H}_2\text{O} = \text{CO} + 3\text{H}_2$	-13.78	-17.80	-4.46	-8.13	-3.08	-1.79
$\text{CaCO}_3(\text{cc}) + \text{H}_2\text{O} = \text{Ca}(\text{OH})_2(\text{po}) + \text{CO}_2$	-5.60	-6.23	-3.49	-3.09	-1.89	-1.63
$\text{Ca}(\text{OH})_2(\text{po}) = \text{Ca}^{2+} + 2\text{OH}^-$	-8.29	-4.54	-12.11	-5.66	-5.51	-5.39

Notes: Values at 10 kbar for aqueous species were extrapolated from the 5 kbar limit of the slop98.dat database by assuming linearity with the log density of water (see Manning, 2013). Abbreviations: cc = calcite; po = portlandite; aq = aqueous.

and T . The quenched melt was smooth and subglobular. At least one surface of each quenched melt grain was microscopically imprinted with the striated texture of the inner capsule wall (Figs. 2b and 2c). Finally, the quenched melt phase contained an array of cardioid-shaped vesicles with aligned morphologies, suggesting that vapor bubbles were trapped in the melt during quenching.

The final phase assemblage depended primarily on f_{O_2} . Regardless of P or T , experiments at HM, NNO, QFM, and CCO resulted in a final assemblage of calcite+fluid. The inner surfaces of the capsules in these experiments were dusted with additional calcite quench crystals in the form of micrometer-scale rhombohedra that were distributed evenly on all available surfaces (Caciagli and Manning 2003). Experiment CU45, which contained initial $\text{Ca}^{13}\text{CO}_3$ powder, was performed at NNO and contained no $^{13}\text{CH}_4$ in the quench fluid (Fig. 1, Table 1). Regardless of P or T , experiments at the lower f_{O_2} values of IM and WM resulted in a final assemblage that contained portlandite and/or quenched melt. Calcite was sometimes present with portlandite, but never with quenched melt. In some experiments, macroscopic portlandite flakes were aggregated around a residual well-rounded calcite grain (Fig. 2a). Quenched melt was observed in two experiments at WM at 650 and 700 °C, but not at lower T or higher f_{O_2} . Experiment CU29, which contained initial $\text{Ca}^{13}\text{CO}_3$ powder, was

performed at IM and contained abundant $^{13}\text{CH}_4$ in the quench fluid (Fig. 1, Table 1).

Solubility measurements

Solubility data at 700 °C and 10 kbar are shown in Table 3 and Figure 3a. In experiments buffered at f_{O_2} values of QFM and higher, calcite solubility was constant: i.e., independent of f_{O_2} . The average solubility value at QFM and higher was 19.6 ± 5.9 mmolal (± 2 s.d.), within error of the solubility measured in a previous unbuffered experiment at identical P and T (Fig. 3a, open triangle) (Caciagli and Manning 2003). This result is expected because the previously unbuffered experiment was performed at UCLA in the identical graphite-NaCl assembly type in which ambient f_{O_2} has been previously determined to be approximately equal to NNO (Newton and Manning 2005).

Although solubilities were constant at QFM and higher, the values increased as f_{O_2} decreased below QFM. The solubility at WM (experiment S10) was 2–4 times higher than the average value of calcite solubility at QFM and higher (Fig. 3a). As in experiment S10, solubility at WM and 6 kbar (experiment S11, Table 3) was approximately two times greater than calcite solubility at QFM and 10 kbar. This result could not be attributed to a pressure difference because calcite solubility is known to increase with pressure at constant temperature (Caciagli and

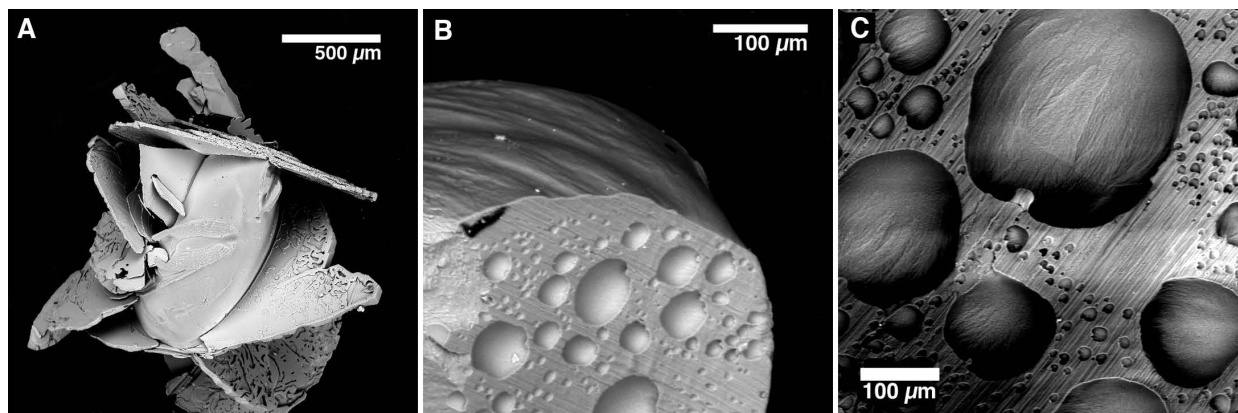


FIGURE 2. SEM images of run products of selected experiments at reducing conditions. (a) Portlandite flakes on a partially dissolved calcite grain (CU28; $f_{\text{O}_2} = \text{IM}$); (b and c) Crystallized melt formed during reaction of calcite. Vesicles and striations are visible on the surface in contact with the inner capsule wall (S11; $f_{\text{O}_2} = \text{WM}$).

TABLE 3. Solubility measurements at 700 °C

Run	Buffer	$\Delta \log Q_{FM}$	$\log f_{O_2}$	P (kbar)	Time (h)	H ₂ O in (mg) ^a	Calcite in (mg) ^a	H ₂ O:CaCO ₃ (molar)	Weight loss (mg) ^b	Solubility (mmolal) ^b	Run products ^c
S10	WM	-4.4	-20.4	10	24	29.5064(4)	0.7043(5)	233	0.1849(2)	62.13(8)	C, P
S11	WM	-4.3	-20.7	6	9	29.0339(6)	0.6697(2)	214	0.1346(2)	45.97(7)	M
S06	QFM	0.0	-16.0	10	8	58.4876(4)	0.5399(2)	600	0.1235(2)	20.93(3)	C
S08	QFM	0.0	-16.0	10	17	30.6549(3)	0.3275(2)	527	0.0589(3)	19.06(9)	C
S02	NNO	0.2	-15.8	10	17	53.7447(18)	1.2232(2)	240	0.1304(4)	24.06(7)	C
S09	NNO	0.2	-15.8	10	17	26.9597(5)	0.2651(2)	554	0.0408(1)	15.02(5)	C
S04	HM	4.0	-12.0	10	8	48.4272(1)	0.7698(2)	339	0.0928(1)	18.99(2)	C
S05	HM	4.0	-12.0	10	12	54.0052(2)	0.6692(3)	266	0.1063(5)	19.52(10)	C

^a Weighing errors are ± 1 s.d. of five repeated measurements. ^b Errors are propagated from ± 1 s.d. weighing errors. ^c Fluid-saturated run products: C = calcite, P = portlandite, M = melt.

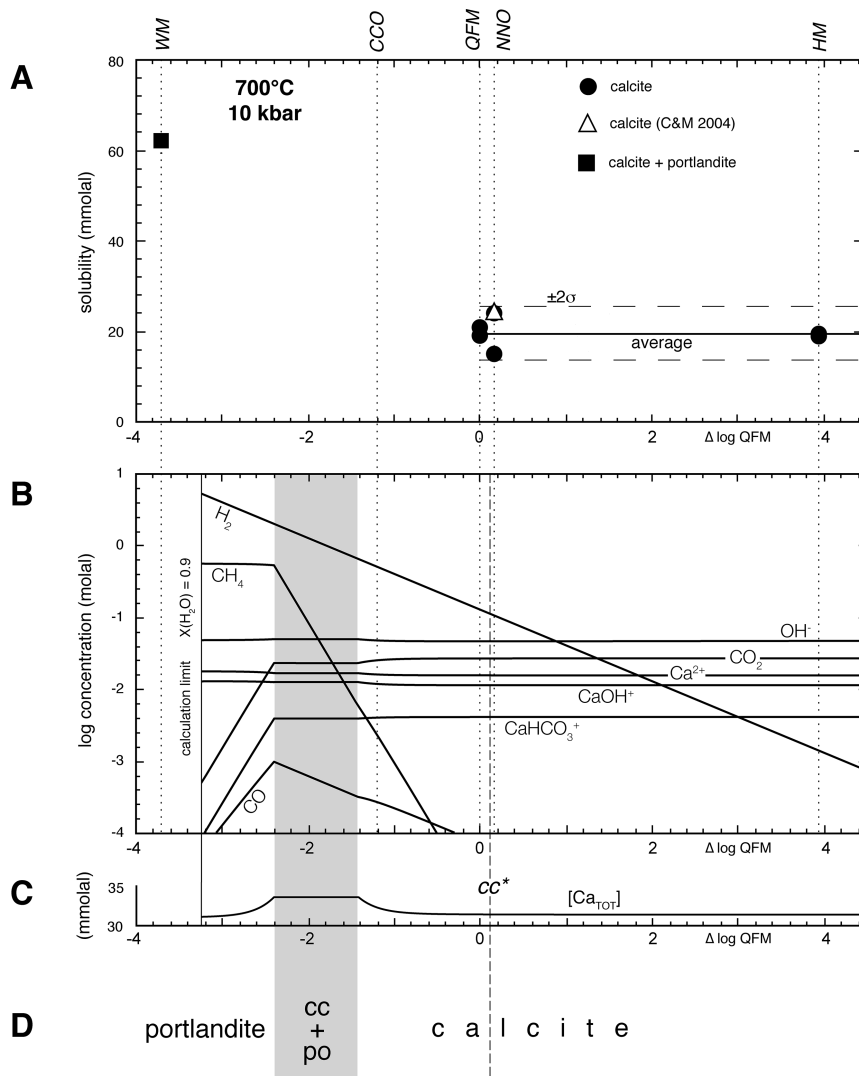


FIGURE 3. Experiments and calculations in the Ca-C-O-H system at 700 °C and 10 kbar. Vertical dotted lines: experimental f_{O_2} buffers WM, CCO, QFM, NNO, and HM. Vertical dashed line: cc^* solubility transition point. Vertical shaded rectangle: calcite+portlandite+fluid stability field. Vertical solid line: limit of calculation, where $X(H_2O) = 0.9$. (a) Solubility measurements from this study and Caciagli and Manning (2003) (C&M 2003). Horizontal lines: average and ± 2 s.d. error envelope of experiments at QFM, NNO, and HM. Individual error bars are not visible at this scale. Because the WM-buffered experiment S11 was performed at 6 kbar, its solubility measurement is not shown. (b) Equilibrium fluid speciation. Species with concentrations below 10^{-4} molal are omitted from the diagram. Water activity is assumed to be unity. (c) Total Ca concentration in fluid, $[Ca_{TOT}]$. (d) Fluid-saturated mineral assemblages; $cc+po$ is calcite+portlandite and is metastable at 700 °C and 10 kbar.

Manning 2003). As will be shown in the Discussion section, the experimental solubilities at WM in S10 and S11 cannot be explained by an equilibrium effect.

Calculations

Thermodynamic calculations permit an exploration of equilibria below 500 °C where equilibrium and redox buffering are kinetically impeded on experimental timescales due to the slow diffusion of H₂ through platinum (Chou et al. 1978; Manning et al. 2013). Moreover, calculations permit the study of equilibria within the region of f_{O_2} space that is experimentally inaccessible due to the unavailability of mineral buffers between CCO and WM/IM.

700 °C and 10 kbar. Figures 3b–3d show the calculated f_{O_2} -dependence of fluid-saturated phase equilibria in the system Ca-C-O-H at 700 °C, 10 kbar, and an initial molar H₂O:CaCO₃ ratio of 100. The results are plotted vs. the parameter $\Delta\log(QFM)$, which is f_{O_2} normalized to QFM at fixed P and T :

$$\Delta\log(QFM) = \log f_{O_2} - \log f_{O_2}(QFM) \quad (3)$$

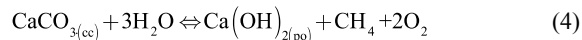
Figure 3b shows the fluid speciation. Figure 3c shows the sum of the concentrations (mmolal) of all Ca-bearing species, [Ca_{TOT}]. The value of [Ca_{TOT}] is controlled by equilibrium between the fluid and the stable mineral assemblages. For example, [Ca_{TOT}] reflects calcite solubility in the calcite+fluid field and portlandite solubility in the portlandite+fluid field. Figure 3d shows the f_{O_2} range over which the assemblages calcite+fluid, calcite+portlandite+fluid ($cc+po$), and portlandite+fluid are stable. In detail, the assemblage calcite+portlandite+fluid may be metastable relative to melt above ~600 °C at 10 kbar (see Discussion); however, for simplification, melt is not considered in the calculation at 700 °C and 10 kbar. To facilitate a discussion of f_{O_2} effects on carbon mobility (see Discussion), the calcite+fluid field is divided into two regions by an f_{O_2} boundary denoted as cc^* . The value of cc^* is defined as the f_{O_2} at which [Ca_{TOT}] is 1% greater than [Ca_{TOT}] at HM relative to the [Ca_{TOT}] plateau within the $cc+po$ field. At f_{O_2} values greater than cc^* , [Ca_{TOT}] is approximately constant; below cc^* , [Ca_{TOT}] increases as f_{O_2} decreases.

Measured calcite solubilities in the f_{O_2} range from QFM to HM were constant, consistent with computed values of [Ca_{TOT}]. This independence of [Ca_{TOT}] with respect to f_{O_2} indicates that, at QFM and higher, calcite-fluid equilibria are primarily governed by O₂-independent reactions involving calcite and aqueous carbonate species. From QFM to HM, the calculated [Ca_{TOT}] value was ~31 mmolal, similar to the average measured value of ~20 mmolal over the same f_{O_2} range.

As f_{O_2} decreases below QFM, the phase assemblages and speciation of the fluid begin to change. Between cc^* and the $cc+po$ field, the stable assemblage remains calcite+fluid, although calcite solubility is no longer independent of f_{O_2} . Calcite solubility increases as [Ca_{TOT}] becomes f_{O_2} -dependent due to the release of Ca and C to the fluid during CaCO₃ reduction, as shown by combining Reactions 1 and 2.

Methane concentration and [Ca_{TOT}] continue to increase as f_{O_2} decreases until portlandite becomes saturated and the system enters the $cc+po$ field. In this field, [Ca_{TOT}] is constant because

decreasing f_{O_2} results in Ca transfer from calcite to portlandite, following the equilibrium



Within the $cc+po$ field, [CH₄] increases as f_{O_2} decreases. Below $\log f_{O_2} \sim -1.7$, [CH₄] is greater than [CO₂]. Thus, although calcite contains oxidized carbon, a calcite-bearing assemblage coexists with a CH₄-rich fluid within the $cc+po$ field. With further decrease in f_{O_2} within the $cc+po$ field, calcite is consumed until it disappears at the high f_{O_2} boundary of the portlandite+fluid field. The f_{O_2} value for this calcite-out boundary is fixed by the bulk composition of the system (see below).

Within the portlandite+fluid field, CH₄ is approximately constant and unaffected by f_{O_2} because portlandite is C-free and methane is by far the most abundant species in the fluid. Therefore, [CH₄] within the portlandite+fluid field may be derived directly from knowledge of the bulk fraction of carbon in the system. Values for [Ca_{TOT}] in the portlandite+fluid field are controlled by portlandite solubility and are f_{O_2} -dependent near the $cc+po$ boundary, primarily owing to reduction of CaHCO₃⁺.

300 °C and 500 °C. Figure 4 shows the results of thermodynamic calculations in the Ca-C-O-H system at 300–500 °C, 2–10 kbar, and H₂O:CaCO₃ = 100. For ease of viewing, only species containing C or Ca are shown. The maximum [CH₄] is the same in all diagrams, as defined by the bulk carbon composition.

Although variations in fluid speciation are chiefly dependent on f_{O_2} , they also depend to a lesser degree on P and T . Within the cc region, the dominant C-species is CO₂, except at 300 °C and 10 kbar where CaCO_{3(aq)}} is the most abundant species. The species CaHCO₃⁺ is favored at higher pressures and Ca(OH)⁺ is favored at higher temperatures. Carbon monoxide is present in minor to trace concentrations. The concentrations of some species change nonlinearly. For example, at 10 kbar, the ratio [CaOH⁺]/[Ca²⁺] at oxidized conditions shows a maximum at 500 °C relative to 300 and 700 °C (compare to Fig. 3b).

The plots illustrate the pressure dependence of calcite solubility, as shown by the substantial increase in the concentration of C- and Ca-bearing species in the calcite+fluid field from 2 to 10 kbar. With the caveat that the thermodynamic properties of portlandite dissolution are extrapolated to 10 kbar, portlandite solubility also increases with pressure, as shown by the increase in [Ca_{TOT}] within the portlandite+fluid field from 2 to 10 kbar.

Bulk composition effects. The minimum f_{O_2} of calcite stability, equivalent to the low f_{O_2} limit of the $cc+po$ field, depends on the total fraction of carbon in the bulk system, as parameterized by the ratio H₂O:CaCO₃. This concept is illustrated with a pair of calculations at 650 °C and 10 kbar (Fig. 5). As H₂O:CaCO₃ decreases and the fraction of total carbon in the system increases, the $cc+po$ field expands to lower f_{O_2} . In other words, as the fraction of bulk CaCO₃ increases, the value of [H₂] required to destabilize calcite also increases.

Bulk composition also controls the maximum carbon concentration in the fluid, which occurs within the portlandite+fluid field. Because calcite is not stable, all the carbon in the system is partitioned into the fluid, and carbon concentration is directly correlated to the total carbon. Graphite saturation could limit carbon concentration below the maximum possible value;

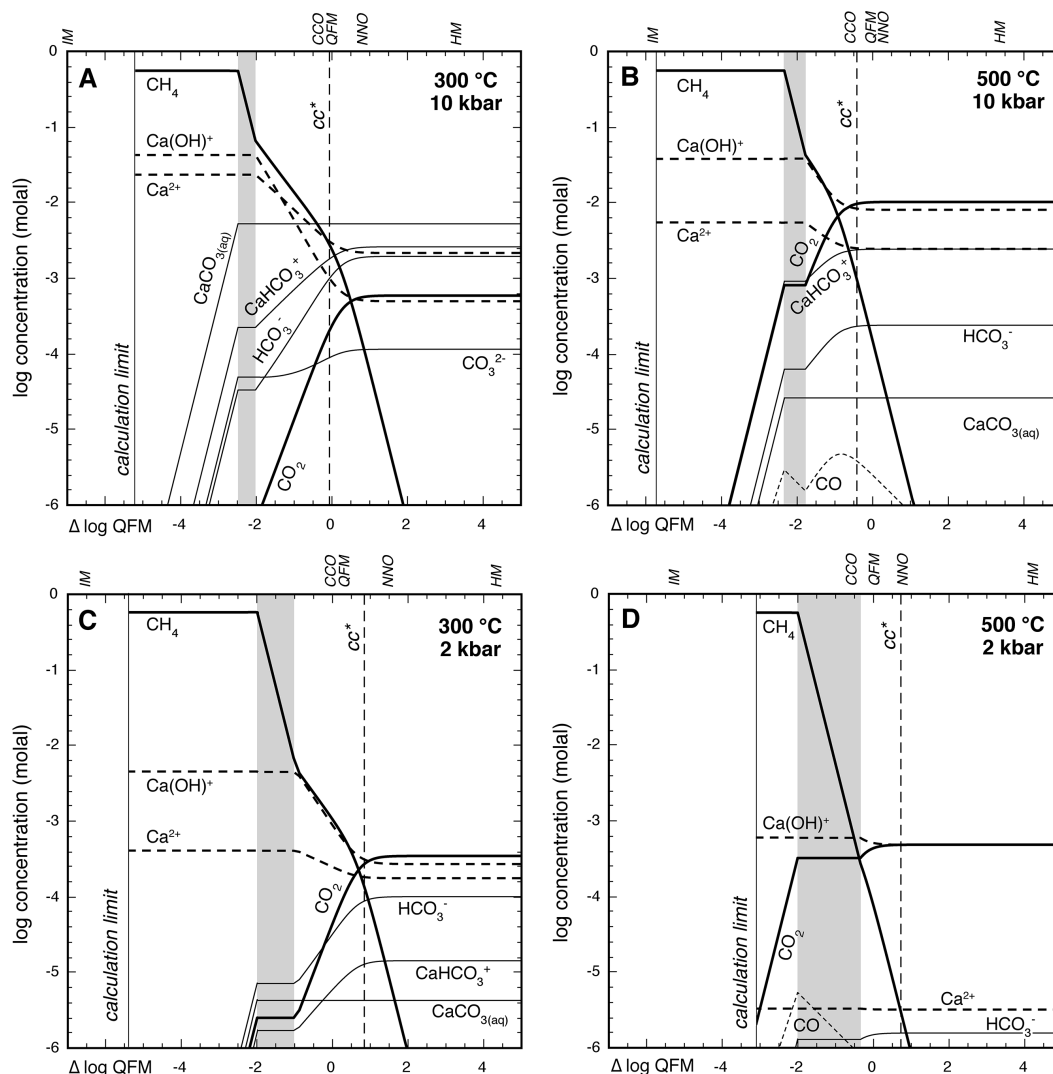


FIGURE 4. Equilibrium fluid speciation calculations in the Ca-C-O-H system. Only Ca- and C-bearing species are shown. Experimental f_{O_2} buffers WM, CCO, QFM, NNO, and HM are denoted above each figure. Vertical dashed line: cc^* solubility transition point. Vertical shaded rectangle: calcite+portlandite+fluid stability field. Vertical solid line: limit of calculation, where $X(H_2O) = 0.9$. This figure may be compared to Figure 3b, although the vertical scales differ.

however, graphite saturation is impeded at low f_{O_2} except when the mole fraction of carbon in the fluid is very high (see Discussion).

The range in bulk composition in the present experiments is substantial, with $H_2O:CaCO_3$ ranging from 11 to 600. Such variations, however, did not affect the experimental outcomes (Fig. 5). The only phase boundary affected by bulk composition is the lower f_{O_2} limit of the $cc+po$ field; however, each experiment was performed at an f_{O_2} value far from this limit, well within either the calcite+fluid or the portlandite+fluid fields. This may be illustrated by inspection of experiment CU29, the most C-rich of all portlandite-generating experiments, where $H_2O:CaCO_3 = 43$ and f_{O_2} was buffered at WM. At the conditions shown in Figure 5, the $\Delta\log(QFM)$ value of WM is -4.15 ,

approximately 1.5 log units below the lower f_{O_2} limit of $cc+po$ at $H_2O:CaCO_3 = 30$.

DISCUSSION

Although reversals were not performed (i.e., no experiments were conducted with starting portlandite), the experiments that resulted in a final assemblage of calcite+fluid or portlandite+fluid were likely equilibrated. First, each of these post-run assemblages was consistent with that predicted from the calculations. Second, previous solubility measurements suggest that the calcite+fluid assemblage equilibrates in less than 12 h at oxidizing conditions similar to those of our study (Caciagli and Manning 2003). Furthermore, agreement between solubility measurements at 8 and 17 h in the current study (experiments S06 and S08) suggests

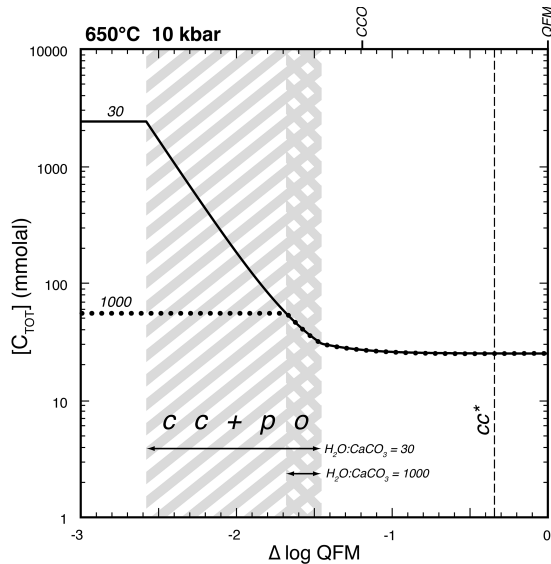


FIGURE 5. Effect of bulk composition on the behavior of total carbon in solution, $[C_{TOT}]$, and the width of the calcite+portlandite+fluid field ($cc+po$) at 650 °C and 10 kbar. The WM buffer at these conditions is $\Delta \log(QFM) = -4.15$. Vertical dashed line: cc^* solubility transition point. Vertical striped-shaded regions: calcite+portlandite+fluid ($cc+po$) stability fields. The bulk $H_2O:CaCO_3 = 30$ is represented by the solid line for $[C_{TOT}]$ and the NE-SW trending striped $cc+po$ region. The bulk $H_2O:CaCO_3 = 1000$ is represented by the dotted line for $[C_{TOT}]$ and the NW-SE trending striped $cc+po$ region.

that calcite-fluid equilibrium occurred in less than 8 h. Finally, early experimental work in the Ca-C-O-H system (Wyllie and Tuttle 1960; Wyllie and Boettcher 1969) indicates that calcite-portlandite equilibration occurs in less than 8 h, with phase transformations occurring in minutes at P and T conditions of the current study.

A possible complication to rapid equilibration is that calcite reduction is tied to aqueous abiotic methanogenesis, a process known to be experimentally sluggish at low-grade hydrothermal conditions (McCollom and Seewald 2001). Therefore, in some cases post-run calcite may have been metastable if methanogenesis were kinetically inhibited. However, no experiment containing post-run calcite+fluid was performed at an f_{O_2} value where CH_4 was calculated to be a significant species in the fluid. Moreover, platinum, present in the inner capsules, is an effective industrial methane catalyst (Rofederpoorter 1981). Coupled with high CH_4/CO_2 in the quench gas of an experiment at IM (CU29) and portlandite formation within 1–2 h at 650–700 °C (experiments CG06 and CU13), it appears that suppression of methane did not occur.

Several experiments resulted in assemblages that were not predictable from equilibrium calculations. The equilibrium assemblage at IM or WM is portlandite+fluid at all P and T in the study; however, several experiments performed at WM (CG10, CU13, CU28, and S10) contained calcite+portlandite+fluid in the run products. These results may be explained by the interpretation that calcite was unstable, and that reduction of calcite to portlandite was incomplete in these experiments. Calcite instability

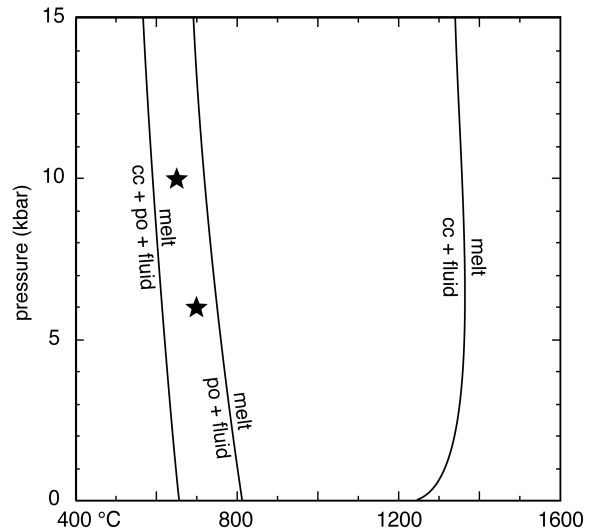


FIGURE 6. Hydrous melting curves in the Ca-C-O-H system from Wyllie and Boettcher (1969). Filled stars represent experiments in which melt was generated via reduction.

also explains the elevated solubility measurement in experiment S10 (Fig. 3a). Because the molecular weight of calcite is greater than the molecular weight of portlandite, conversion of calcite to portlandite and methane (see reaction 4) implies a net weight loss to the fluid. The weight loss in experiment S10, therefore, is likely proportional to the fraction of initial unstable calcite that was reacted to form portlandite.

Incomplete reduction of calcite to portlandite also led to melting in experiments of short duration. We interpret this melting to be metastable for the following reasons. Both experiments containing quenched melt, CG06 and S11, were performed at WM, well within the portlandite+fluid stability field at all experimental conditions. However, these experiments were performed at P - T conditions below the hydrous melting curve of portlandite (Fig. 6; Wyllie and Boettcher 1969). Moreover, experiments at WM of longer duration did not yield a quenched melt. Because the P - T conditions of the quenched melt experiments were above the hydrous calcite+portlandite melting curve (Fig. 6), melting may be explained by incomplete conversion of calcite to portlandite, i.e., a metastable freezing point depression. An important caveat is that the Wyllie and Boettcher curves (1969) were derived from experiments at oxidized conditions. A reduction in water activity due to H_2 formation at WM would have expanded the portlandite+fluid region, making melting less likely. However, the fact that quenched melt was generated in the two experiments indicates that, even if a shift in the hydrous melting curve occurred due to reduced water activity, the extent of such a shift did not suppress metastable melting.

Although melting in the present experiments was interpreted to be metastable, the calculations imply the existence of conditions at which reduction of calcite to portlandite could generate a stable melt. Our calculations do not explicitly account for a melt phase; however, to a first order, a melt stability field may approximately overlap the metastable extension of the $cc+po$ field beyond the hydrous calcite+portlandite melting curve. Redox

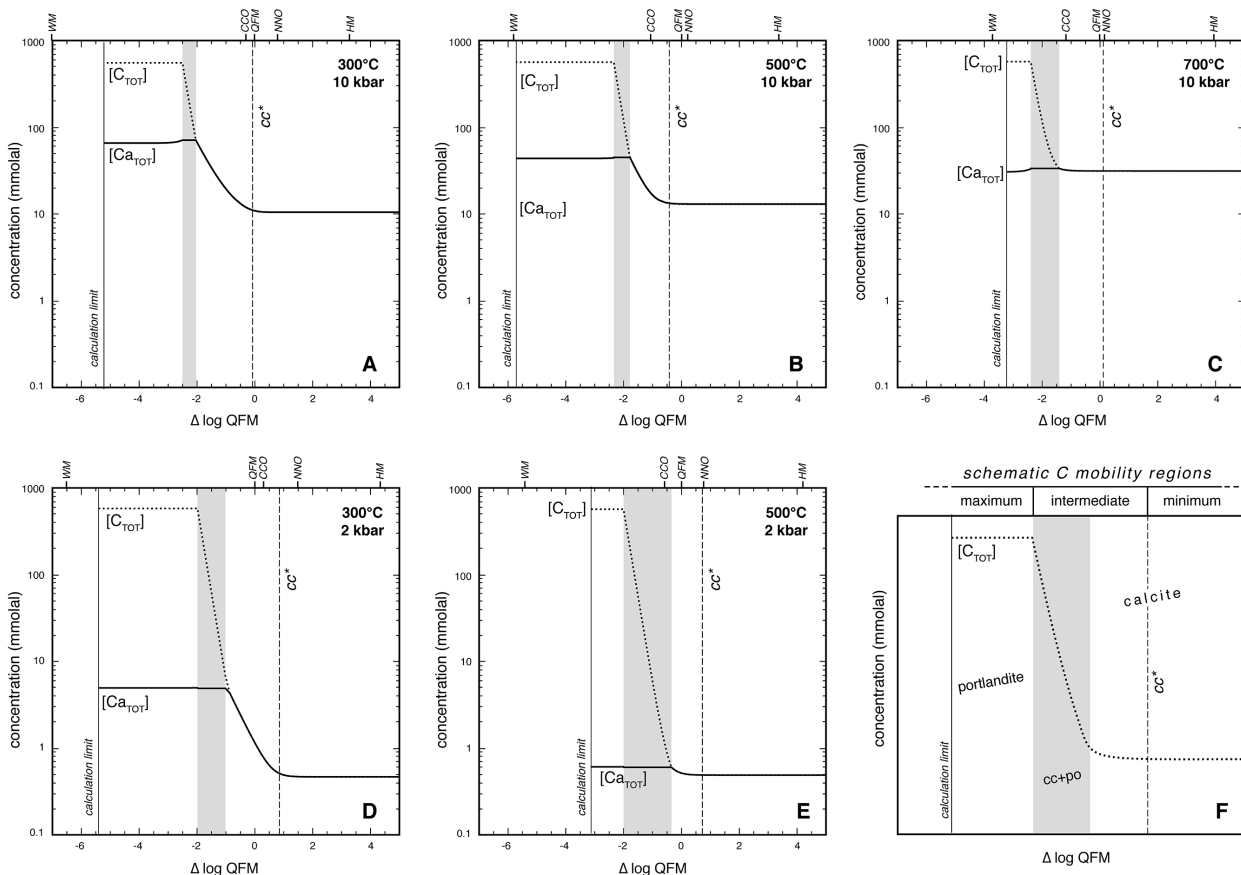


FIGURE 7. Carbon and calcium in equilibrated Ca-C-O-H fluids. Vertical dashed line: cc^* solubility transition point. Vertical shaded rectangle: calcite+portlandite+fluid stability field (metastable in C). Vertical solid line: limit of calculation, where $X(H_2O)=0.9$. (a–e) Total carbon concentration ($[C_{TOT}]$, dotted lines) and total calcium concentration ($[Ca_{TOT}]$, solid lines). (f) Schematic $[C_{TOT}]$ diagram showing schematic carbon mobility regions.

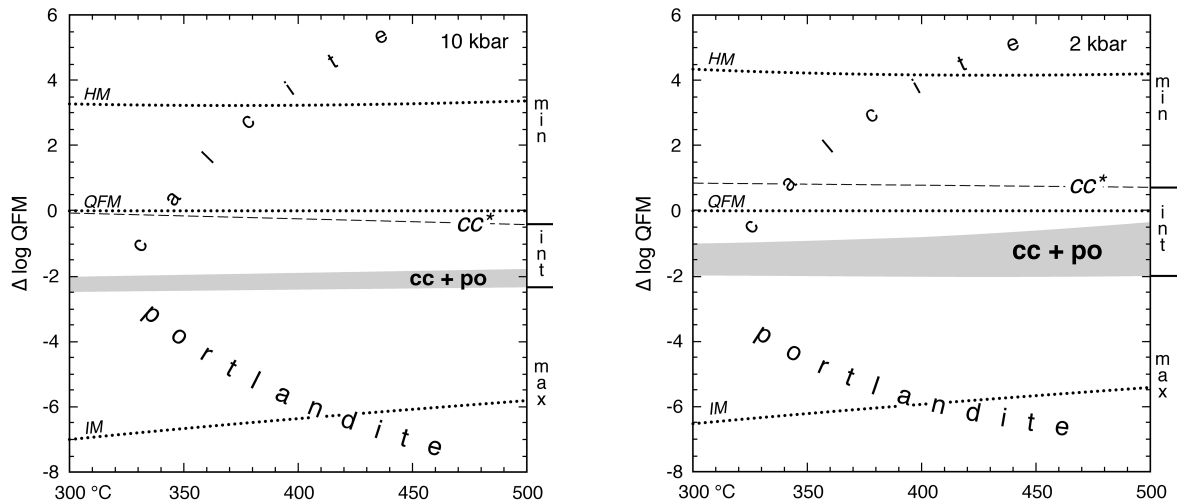


FIGURE 8. Effect of pressure on redox-dependent phase equilibria in the Ca-C-O-H system, 300–500 °C, 2 and 10 kbar. Dashed lines: cc^* solubility transition point. Dotted lines: experimental f_{O_2} buffers IM, QFM, and HM. Shaded regions: calcite+portlandite+fluid stability field ($cc+po$). Carbon mobility regions are plotted on right axes.

melting, i.e., melting that occurs upon a change in the oxidation state of a system, has been previously associated with oxidation processes: e.g., basaltic magma genesis during oxidation of CH_4 to CO_2 and H_2O in the mantle wedge (Song et al. 2009) and formation of carbonatite melts during oxidation of diamond to CO_2 in the upper mantle (Rohrbach and Schmidt 2011). However, the melting of calcite considered here occurs during reduction. Such a process could occur in subduction zones if serpentinite-derived H_2 -rich fluids infiltrate carbonate lithologies.

IMPLICATIONS

The redox dependence of fluid speciation and phase stabilities in the Ca-C-O-H system has important implications for carbon mobility (Figs. 7–8). To illustrate, three regions of carbon mobility are defined, shown schematically in Figure 7f: maximum, intermediate, and minimum. The region of maximum carbon mobility occurs at low f_{O_2} in the portlandite+fluid field, where carbon is perfectly mobile. Here, calcite is not stable and all of the carbon in the system is contained in the fluid, mostly as CH_4 . The region of minimum carbon mobility occurs at oxidized conditions in the calcite+fluid field at f_{O_2} values greater than cc^* . Within this region, $[\text{C}_{\text{TOT}}]$ is limited by calcite-fluid equilibria, i.e., no carbon is partitioned into the fluid in excess of that fixed by equilibrium calcite solubility. The region of intermediate carbon mobility is defined as the range in which $[\text{C}_{\text{TOT}}]$ increases continuously as f_{O_2} decreases from cc^* to the upper f_{O_2} boundary of the portlandite+fluid field. Within this range, $[\text{C}_{\text{TOT}}]$ increases as $[\text{CH}_4]$ increases by partial reduction of calcite to portlandite. As explained in the previous section, the low f_{O_2} limit of the region of intermediate carbon mobility migrates to lower f_{O_2} as

$\text{H}_2\text{O}:\text{CaCO}_3$ decreases. Independent of fluid-rock ratio, fluids that equilibrate within the intermediate and/or maximum mobility regions may be said to have reduction-enhanced carbon mobility.

Maximum carbon mobility occurs in highly reduced geological fluids. Over the range of P and T in Figures 7 and 8, the upper f_{O_2} limit of the region of maximum mobility is approximately two log units below QFM. This reduced state may be attained during many natural terrestrial petrologic processes such as hydrous metamorphism of Fe-rich silicates (Eugster and Wones 1962; Frost 1979), accumulation of radiolytic H_2 in Precambrian shields (Lin et al. 2005), basalt diking in coal deposits (Klöck et al. 1986) and equilibrium in the lower mantle (Frost et al. 2004). However, the most common highly reducing geologic process in the lithosphere is serpentinization, which can buffer f_{O_2} to up to seven log units below QFM (Frost 1985).

Carbon mobility in fluids may also be reduction-enhanced, albeit to a lesser degree, at redox conditions that are less extreme than the f_{O_2} values of highly reducing serpentinization. For example, during low-grade metamorphism (e.g., 300 °C and 2 kbar), QFM lies within the intermediate mobility region (Fig. 7d). Because hydrothermal alteration of terrestrial basalt is commonly thought to proceed at redox conditions at or near QFM (Lyons et al. 2005), this implies that carbon mobility is reduction-enhanced during basaltic metamorphism.

Pressure and temperature affect the range of redox conditions of the intermediate carbon mobility region, with consequences for the variety of natural geological processes in which reduction-enhanced carbon mobility is possible. As pressure increases, QFM becomes more oxidizing than cc^* , the upper f_{O_2} limit of the region of intermediate mobility; i.e., the maximum f_{O_2} of reduction-

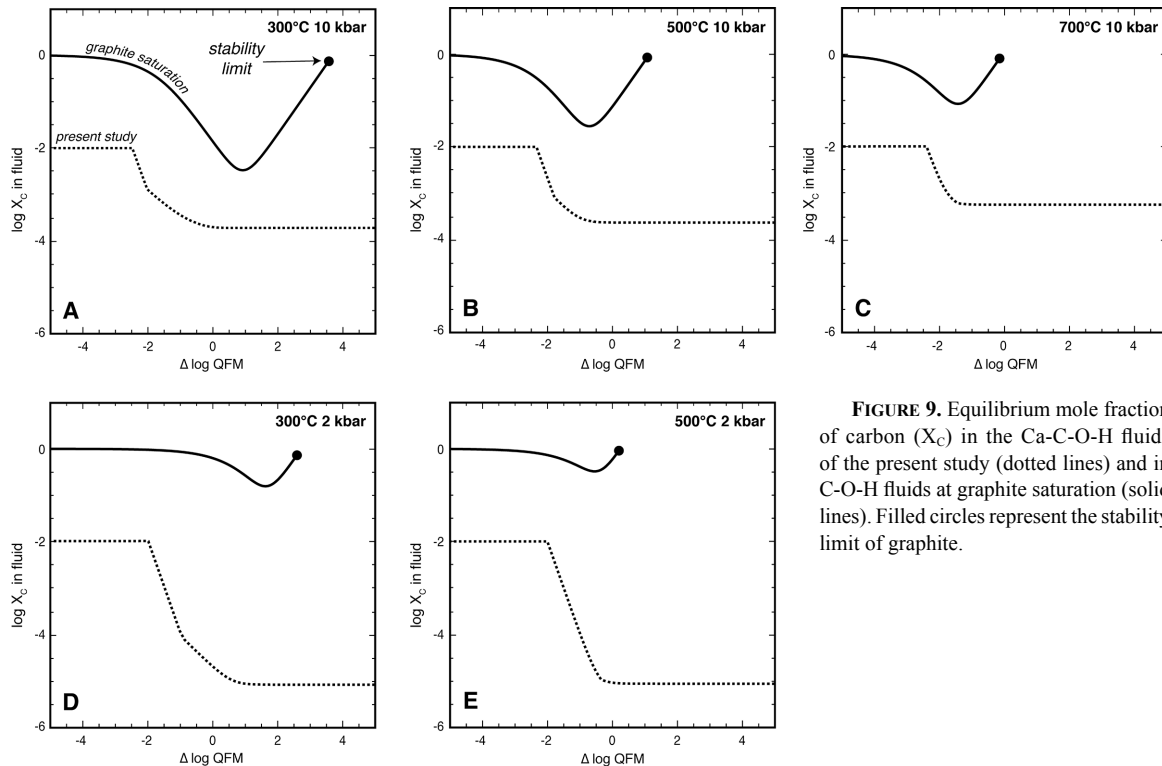


FIGURE 9. Equilibrium mole fraction of carbon (X_c) in the Ca-C-O-H fluids of the present study (dotted lines) and in C-O-H fluids at graphite saturation (solid lines). Filled circles represent the stability limit of graphite.

enhanced carbon mobility decreases with increasing pressure. For example, at 2 kbar, QFM is sufficiently reducing that its f_{O_2} value lies within the intermediate mobility region from 300–500 °C (Fig. 8b), whereas QFM at 10 kbar lies within the minimum mobility region (Fig. 8a). This result indicates that the potential for basaltic metamorphism to result in reduction-enhanced carbon mobility decreases with increasing depth in geological systems. Basaltic metamorphism at very low pressures (<500 bars) attending hydrothermal alteration in mid-ocean ridge systems may result in reduction-enhanced carbon mobility. At moderate to high metamorphic grades within subduction zones, serpentinization may be the only common fluid-rock process with the ability to generate fluids with reduction-enhanced carbon concentrations.

A recent report of graphite in eclogite-blueschist marble formed during reduction of carbonate by serpentinite-derived H_2 (Malvoisin et al. 2012) suggests that carbon mobility in subduction zones could be limited by graphite saturation. However, carbon concentration in a graphite-saturated fluid is very high, implying that carbon is highly mobile in reduced fluids with or without graphite. This may be illustrated by comparing the mole fraction of carbon (X_C) in fluids at graphite saturation to X_C in fluids at calcite and/or portlandite saturation in the model Ca-C-O-H system. The results are plotted in Figure 9, at conditions identical to Figure 7, and show that X_C at graphite saturation exceeds X_C in the model Ca-C-O-H system for all values of f_{O_2} . Graphite saturation could be promoted in the low f_{O_2} portlandite+fluid region by increasing X_C in the model system (i.e., decreasing $H_2O:CaCO_3$), implying that graphite saturation is associated with increased, not decreased, carbon mobility.

Because carbon mobility increases primarily due to an increase in methane concentration, calcite reduction could be a productive mechanism for abiotic methanogenesis, an important astrobiological and geochemical process (McCollom and Seewald 2007). If calcite is abundant in or near serpentinites in subduction zones, then methanogenesis via calcite reduction may be ubiquitous in subducted oceanic lithosphere. In support of this inference, several recent papers have reported CH_4 -rich, CO_2 -poor fluid inclusions with likely abiotic origins in subducted ultramafic lithologies (Shi et al. 2005; Liu and Fei 2006; Sachan et al. 2007; Song et al. 2009). Even in the absence of reduction, carbon mobility in subduction zones is likely high, owing to the substantial pressure enhancement of calcite solubility in aqueous fluids (Caciagli and Manning 2003; Facq et al. 2014). However, the additional effect of carbonate reduction implies that subduction zones may host some of the most C-rich fluids in the global geological carbon cycle.

ACKNOWLEDGMENTS

The authors thank Sarah Penniston-Dorland for thoughtful editorial handling, and Christopher Oze, Nadia Malaspina, and an anonymous reviewer for helpful comments. The authors also thank Cathleen Brown and the Department of Mineral Sciences at the Smithsonian Institution for providing calcite, John Armstrong for assistance with SEM, George Cody for assistance with GCMS analyses, and Bob Newton and Dimitri Sverjensky for helpful discussions. The work was partly supported by grants from NSF EAR-1049901 and the Deep Carbon Observatory.

REFERENCES CITED

- Anderson, G.M., and Crerar, D.A.A. (1993) *Thermodynamics in Geochemistry: The Equilibrium Model*. Oxford University Press, U.K.
- Caciagli, N.C., and Manning, C.E. (2003) The solubility of calcite in water at 6–16 kbar and 500–800 °C. *Contributions to Mineralogy and Petrology*, 146, 275–285.
- Chou, I.M., Eugster, H.P., Berens, P., and Weare, J.H. (1978) Diffusion of hydrogen through platinum membranes at high-pressures and temperatures. *Geochimica et Cosmochimica Acta*, 42, 281–288.
- Davies, C.W. (1962) *Ion Association*. 190 p. Butterworth, Washington, D.C.
- Dobson, D.P., Jones, A.P., Rabe, R., Sekine, T., Kurita, K., Taniguchi, T., Kondo, T., Kato, T., Shimomura, O., and Urakawa, S. (1996) In-situ measurement of viscosity and density of carbonate melts at high pressure. *Earth and Planetary Science Letters*, 143, 207–215.
- Dolejš, D., and Manning, C.E. (2010) Thermodynamic model for mineral solubility in aqueous fluids: theory, calibration and application to model fluid-flow systems. *Geofluids*, 10, 20–40.
- Eugster, H.P. (1957) Heterogeneous reactions involving oxidation and reduction at high pressures and temperatures. *Journal of Chemical Physics*, 26, 1760–1761.
- Eugster, H.P., and Wones, D.R. (1962) Stability relations of the ferruginous biotite, annite. *Journal of Petrology*, 3, 82–125.
- Evans, B.W. (2010) Lizardite versus antigorite serpentinite; magnetite, hydrogen, and life(?). *Geology*, 38, 879–882.
- Facq, S., Daniel, I., Montagnac, G., Cardon, H., and Sverjensky, D.A. (2014) In situ Raman study and thermodynamic model of aqueous carbonate speciation in equilibrium with aragonite under subduction zone conditions. *Geochimica et Cosmochimica Acta*, 132, 375–390.
- Fein, J.B., and Walther, J.V. (1989) Calcite solubility and speciation in supercritical NaCl-HCl aqueous fluids. *Contributions to Mineralogy and Petrology*, 103, 317–324.
- French, B.M. (1966) Some geological implications of equilibrium between graphite and a C-H-O gas phase at high temperatures and pressures. *Reviews of Geophysics*, 4, 223–253.
- Frost, B.R. (1979) Metamorphism of iron-formation; parageneses in the system Fe-Si-C-O-H. *Economic Geology*, 74, 775–785.
- (1985) On the stability of sulfides, oxides, and native metals in serpentinite. *Journal of Petrology*, 26, 31–63.
- Frost, B.R., and Beard, J.S. (2007) On silica activity and serpentinization. *Journal of Petrology*, 48, 1351–1368.
- Frost, D.J., Liebske, C., Langenhorst, F., McCammon, C.A., Tronnes, R.G., and Rubie, D.C. (2004) Experimental evidence for the existence of iron-rich metal in the Earth's lower mantle. *Nature*, 428, 409–412.
- Galvez, M.E., Martinez, I., Beyssac, O., Benzerara, K., Agrinier, P., and Assayag, N. (2013) Metasomatism and graphite formation at a lithological interface in Malaspina (Alpine Corsica, France). *Contributions to Mineralogy and Petrology*, 166, 1687–1708.
- Giardini, A., Salotti, C., and Lakner, J. (1968) Synthesis of graphite and hydrocarbons by reaction between calcite and hydrogen. *Science*, 159, 317–319.
- Helgeson, H.C., Delany, J.M., Nesbitt, H.W., and Bird, D.K. (1978) Summary and critique of the thermodynamic properties of rock-forming minerals. *American Journal of Science*, 278, 1–229.
- Holland, T., and Powell, R. (1991) A Compensated Redlich-Kwong (CORK) equation for volumes and fugacities of CO_2 and H_2O in the range 1-bar to 50-kbar and 100–1600-degrees-C. *Contributions to Mineralogy and Petrology*, 109, 265–273.
- Hunter, R.H., and McKenzie, D. (1989) The equilibrium geometry of carbonate melts in rocks of mantle composition. *Earth and Planetary Science Letters*, 92, 347–356.
- Hyndman, R.D., and Peacock, S.M. (2003) Serpentinization of the forearc mantle. *Earth and Planetary Science Letters*, 212, 417–432.
- Klöck, W., Palme, H., and Tobschall, H.J. (1986) Trace elements in natural metallic iron from Disko Island, Greenland. *Contributions to Mineralogy and Petrology*, 93, 273–282.
- Lécuyer, C., and Ricard, Y. (1999) Long-term fluxes and budget of ferric iron: implication for the redox states of the Earth's mantle and atmosphere. *Earth and Planetary Science Letters*, 165, 197–211.
- Lin, L.H., Slater, G.F., Lollar, B.S., Lacrampe-Couloume, G., and Onstott, T.C. (2005) The yield and isotopic composition of radiolytic H_2 , a potential energy source for the deep subsurface biosphere. *Geochimica et Cosmochimica Acta*, 69, 893–903.
- Liu, W., and Fei, P.X. (2006) Methane-rich fluid inclusions from ophiolitic dunite and post-collisional mafic-ultramafic intrusion: The mantle dynamics underneath the Palaeo-Asian Ocean through to the post-collisional period. *Earth and Planetary Science Letters*, 242, 286–301.
- Lyons, J.R., Manning, C., and Nimmo, F. (2005) Formation of methane on Mars by fluid-rock interaction in the crust. *Geophysical Research Letters*, 32, L13201, doi:10.1029/2004GL022161.
- Malvoisin, B., Chopin, C., Brunet, F., and Galvez, M.E. (2012) Low-temperature wollastonite formed by carbonate reduction: a marker of serpentinite redox conditions. *Journal of Petrology*, 53, 159–176.
- Manning, C.E. (2013) Thermodynamic modeling of fluid-rock interaction at mid-crustal to upper-mantle conditions. *Reviews in Mineralogy and Geochemistry*, 76, 135–164.
- Manning, C.E., Shock, E.L., and Sverjensky, D.A. (2013) The chemistry of carbon in aqueous fluids at crustal and upper-mantle conditions: experimental and

- theoretical constraints. *Reviews in Mineralogy and Geochemistry*, 75, 109–148.
- Marshall, W.L., and Franck, E.U. (1981) Ion product of water substance, 0–1000 °C, 1–10,000 bars: New International Formulation and its background. *Journal of Physical and Chemical Reference Data*, 10, 295–304.
- McCollom, T.M., and Seewald, J.S. (2001) A reassessment of the potential for reduction of dissolved CO₂ to hydrocarbons during serpentinization of olivine. *Geochimica et Cosmochimica Acta*, 65, 3769–3778.
- (2007) Abiotic synthesis of organic compounds in deep-sea hydrothermal environments. *Chemical Reviews*, 107, 382.
- Minarik, W.G., and Watson, E.B. (1995) Interconnectivity of carbonate melt at low melt fraction. *Earth and Planetary Science Letters*, 133, 423–437.
- Morgan, J.K., and Milliken, K.L. (1996) Petrography of calcite veins in serpentinized peridotite basement rocks from the Iberia Abyssal Plain, Sites 897 and 899: kinematic and environmental implications. In R.B. Whitmarsh, D.S. Sawyer, A. Klaus, and D.G. Masson, Eds. *Proceedings of the Ocean Drilling Program, Scientific results*, 149, 559–569, College Station, Texas.
- Newton, R.C., and Manning, C.E. (2002) Experimental determination of calcite solubility in H₂O-NaCl solutions at deep crust/upper mantle pressures and temperatures: Implications for metasomatic processes in shear zones. *American Mineralogist*, 87, 1401–1409.
- (2005) Solubility of anhydrite, CaSO₄, in NaCl-H₂O solutions at high pressures and temperatures: Applications to fluid-rock interaction. *Journal of Petrology*, 46, 701–716.
- Peacock, S.M. (1990) Fluid processes in subduction zones. *Science*, 248, 329–337.
- Peretti, A., Dubessy, J., Mullis, J., Frost, B.R., and Trommsdorff, V. (1992) Highly reducing conditions during Alpine metamorphism of the Malenco Peridotite (Sondrio, Northern Italy) indicated by mineral paragenesis and H₂ in fluid inclusions. *Contributions to Mineralogy and Petrology*, 112, 329–340.
- Referdepoorter, C.K. (1981) A comprehensive mechanism for the Fischer-Tropsch synthesis. *Chemical Reviews*, 81, 447–474.
- Rohrbach, A., and Schmidt, M.W. (2011) Redox freezing and melting in the Earth's deep mantle resulting from carbon-iron redox coupling. *Nature*, 472, 209–212.
- Sachan, H.K., Mukherjee, B.K., and Bodnar, R.J. (2007) Preservation of methane generated during serpentinization of upper mantle rocks: Evidence from fluid inclusions in the Nidar ophiolite, Indus Suture Zone, Ladakh (India). *Earth and Planetary Science Letters*, 257, 47–59.
- Sano, Y., and Williams, S.N. (1996) Fluxes of mantle and subducted carbon along convergent plate boundaries. *Geophysical Research Letters*, 23, 2749–2752.
- Schmidt, M.W., and Poli, S. (1998) Experimentally based water budgets for dehydrating slabs and consequences for arc magma generation. *Earth and Planetary Science Letters*, 163, 361–379.
- Shi, G.U., Tropper, P., Cui, W.Y., Tan, J., and Wang, C.Q. (2005) Methane, (CH₄)-bearing fluid inclusions in the Myanmar jadeiteite. *Geochemical Journal*, 39, 503–516.
- Shock, E.L., Helgeson, H.C., and Sverjensky, D.A. (1989) Calculation of the thermodynamic and transport properties of aqueous species at high pressures and temperatures: Standard partial molal properties of inorganic neutral species. *Geochimica et Cosmochimica Acta*, 53, 2157–2183.
- Shock, E.L., Sassani, D.C., Willis, M., and Sverjensky, D.A. (1997) Inorganic species in geologic fluids: Correlations among standard molal thermodynamic properties of aqueous ions and hydroxide complexes. *Geochimica et Cosmochimica Acta*, 61, 907–950.
- Song, S.G., Su, L., Niu, Y.L., Lai, Y., and Zhang, L.F. (2009) CH₄ inclusions in orogenic harzburgite: Evidence for reduced slab fluids and implication for redox melting in mantle wedge. *Geochimica et Cosmochimica Acta*, 73, 1737–1754.
- Ulmer, P., and Trommsdorff, V. (1995) Serpentine stability to mantle depths and subduction-related magmatism. *Science*, 268, 858–861.
- Walther, J.V. (1986) Experimental determination of portlandite and brucite solubilities in supercritical H₂O. *Geochimica et Cosmochimica Acta*, 50, 733–739.
- Walther, J.V., and Long, M.I. (1986) Experimental determination of calcite solubilities in supercritical H₂O. 5th International Symposium on Water-Rock Interaction, 5:609–611.
- Wyllie, P.J., and Boettcher, A.L. (1969) Liquidus phase relationships in system CaO-CO₂-H₂O to 40 kilobars pressure with petrological applications. *American Journal of Science*, 267, 489–508.
- Wyllie, P.J., and Tuttle, O.F. (1960) The system CaO-CO₂-H₂O and the origin of carbonatites. *Journal of Petrology*, 1, 1–46.

MANUSCRIPT RECEIVED JULY 26, 2013

MANUSCRIPT ACCEPTED FEBRUARY 22, 2014

MANUSCRIPT HANDLED BY SARAH PENNISTON-DORLAND